An Analytical Model of Earth-Observational Remote Sensing Systems

John P. Kerekes and David A. Landgrebe

Abstract —The field of optical remote sensing for the analysis of Earth's resources has grown tremendously over the past 20 years. With increasing societal concern over such problems as ozone layer depletion and global warming, political support is likely to continue that growth. NASA has recently begun a program that will use state of the art sensor technology and processing algorithms to gain ever more detailed data about our Earth. To better understand the remote sensing process, research has begun on modeling the process as a system and investigating the interrelationships of system components. This paper presents a system model for the remote sensing process and some results that yield insight into its understanding. Key results include interrelationships between the atmosphere, sensor noise, sensor view angle, and scattered path radiance and their influence on classification accuracy of the ground cover type. Also included are results indicating the trade-offs in ground cell size and surface spatial correlation and their effect on classification accuracy.

I. INTRODUCTION

R EMOTE sensing of the Earth's resources from space-based sensors has evolved in the past 20 years from a scientific experiment to a commonly used technological tool. The U.S. Landsat [1], [2] and the French SPOT [3] satellites along with many others have provided a wealth of information about our Earth [4]. NASA has recently begun an international program called Earth Observing System (EOS) to better understand our Earth as a global system [5]. This program will use a complex array of highly sophisticated sensors mounted on polar orbiting platforms to gather detailed data. These sensors will advance the state of the art substantially.

The goals of our research have been twofold. First, it was desired to increase understanding of the remote sensing process through its modeling as a system. By constructing these models we document our knowledge of the remote sensing process as well as provide a sophisticated testbed upon which to build and test theories.

The second goal of our work has been in direct preparation for the use of the next generation of remote sensing satellites. In the use of these instruments scientific investigators will be able to specify many of the observational parameters. It will become increasingly important for the diverse

group of earth scientists who use these tools to have better information available to them about the effects and trade-offs of these observational parameters. Through the use of a system-wide model we can gain insights into these effects and aid in the planning and execution of the scientific experiments.

This paper presents a system-wide model for the study of optical remote sensing systems. In the next section we describe the type of remote sensing systems considered. This is followed by a description of the analytical system model used in our research. Results of the use of this model in the analysis of optical remote sensing systems are then presented before concluding with a summary.

II. REMOTE SENSING SYSTEMS

In our research, the term "remote" sensing is used in the context of satellite- or aircraft-based imaging sensors that produce multispectral digital images of the surface of the Earth for land cover or Earth resource analysis [6]. The imaging sensor covers only the reflective portion of the optical spectrum with wavelengths approximately from 0.4 μm to 2.4 μm. This context includes many of the current and near future remote sensing instruments such as Landsat MSS and TM, SPOT, AVIRIS [7], MODIS [8], and HIRIS [9]. Land cover delineation using the image data represents a significant application of the technology.

A conceptual description of a remote sensing system is given in pictorial form in Fig. 1. This figure gives an overall view of the remote sensing process starting with the illumination provided by the sun. This incoming energy passes through the atmosphere (where it is partially absorbed and scattered) before being reflected from the Earth's surface in a manner presumably indicative of the surface material and its condition. The reflected light then passes again through the atmosphere before entering the input aperture of the sensing instrument.

At the sensor, the incoming optical energy is sampled spatially and spectrally in the process of being converted to an electrical signal. This signal is then amplified and quantized into discrete levels producing a multispectral scene characterization that is then transmitted to the processing facility.

At the processing stage, geometric registration and calibration may be performed on the image in order to be able to compare the data to other data sets. Feature extraction may also be performed to reduce the dimensionality of the data and to increase the separability of the various informational classes in the image. Lastly, the image undergoes a

Fig. 1.   Remote sensing system.

Fig. 2.   System effects block diagram. For each class k of the K classes defined in the scene, the class mean vector and covariance matrix are modified by the function in each of the blocks.

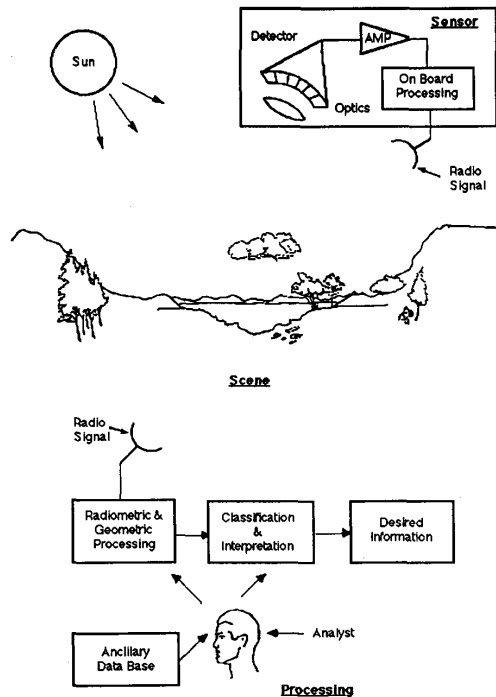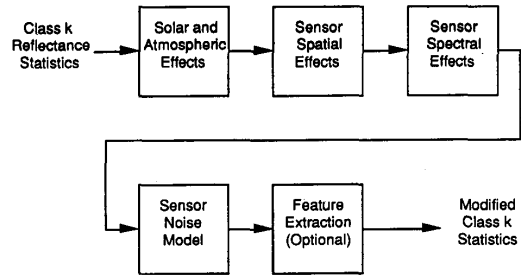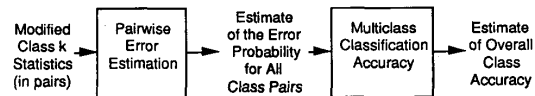Fig. 3.   Accuracy estimation. A pairwise error estimate is made from the modified class statistics and then combined to form an overall classification accuracy estimate.

classification and interpretation stage, most often done with a computer under the supervision of a trained analyst using ancillary information about the scene.

The entire remote sensing process can be viewed as a system whose inputs include a vast variety of sources and forms. Everything from the position of the sun in the sky, the quality of the atmosphere, and the spectral and spatial responses of the sensor to the training fields selected by the analyst, etc., will influence the state of the system. The output of such a system is generally a spatial map assigning each discrete location in the scene to an appropriate land information class. Other outputs may be the amount of area covered by each class in the scene or the classification accuracy, measured by comparing the resulting classified map with the known ground truth of the scene.

In a recent paper we presented an approach to studying these systems using simulation [10]. This approach is useful when simulated images are desirable for processing algorithm study or when detailed spatial effects are necessary for the model. In the study of interrelated parameter effects, the variations introduced by the random number generators require many iterations of the simulation to produce consistent results, and thus such an approach becomes computationally quite intensive.

A simpler and much less computationally intensive approach is one of parametric system analysis. Such a parametric system model was presented in reference [11]. Much of the present work builds on the model developed there. The model we propose varies from this previous work in several important points. As in their work, we use field or laboratory spectra for the surface class reflectance statistics; however,

we introduce the well-developed atmospheric model LOW-TRAN 7 [12] to produce a realistic radiance function. Also, the sensor noise model implemented in our work includes signal dependent shot noise and calibration error. The system model has been implemented in the context of the EOS environment in order to apply the ideas to an upcoming system. Spectral reduction has been applied after the atmospheric and noise effects have been included and a multiclass error estimator, based on the Bhattacharyya distance measure and developed in [13], is used to estimate classification error. The following section describes this model in detail.

III. ANALYTICAL SYSTEM MODEL

A. Model Overview

The analytical system model was built in the context of ground cover classification using multispectral statistics and pattern recognition techniques with the goal of investigating the effect of diverse system parameters on classification accuracy. The model modifies the statistics of each class by system effects before computing an estimate of the classification accuracy based upon an interclass distance measure. Fig. 2 shows a block diagram of the system effects applied to each of the K classes, while Fig. 3 shows the estimation of the classification accuracy based on these modified class statistics.

A brief description of the model follows. Reference [14] contains a full description and a listing of the Fortran implementation of the model. Also, [15] presents an application of the model to the study of the upcoming HIRIS instrument.

B. Surface Reflectance Statistics

The surface reflectance is assumed to be spectrally multivariate Gaussian with a spatial correlation described by a separable exponential model [11]. The multivariate Gaussian

assumption has been shown to be appropriate for the analysis of remotely sensed data [20].

For the examples given in Section IV, the spectral reflectance statistics utilized were computed from a database of field spectra [17] with samples across the optical spectrum from 0.4 to 2.4 μm (with wavelength intervals of 20 to 50 nm). However, other sources of multivariate data (e.g., AVIRIS [7] airborne sensor data converted to reflectance) could be used as well. To take full advantage of the spectral resolution available in the atmospheric model and HIRIS sensor, the data is first interpolated to 10-nm wavelength spacing. Thus, for each class k, the reflectance mean vector $\overline{X}_k$ and the covariance matrix Σ_k will have $M = 201$ dimensions.

The scene is spatially modeled as having cells of constant reflectance (Lambertian assumption) with spatial correlation from cell to cell. The cross-correlation function for wavelengths m and n within a class is shown in (1).

$$R_{mn}(\tau, \eta) = E\{x_m(x, y)x_n(x + \tau, y + \eta)\} = e^{-a_{mn}^{|\tau|}}e^{-b_{mn}^{|\eta|}}.$$
(1)

Here, τ and η are the across- and along-track cell lag values for the spatial correlation function. This form yields spatial cross-correlation coefficients $\rho_{mn,x}$ for across the scene, and $\rho_{mn,y}$ for down scene, as shown in (2) and (3).

$$\rho_{mn,x} = e^{-a_{mn}}$$
(2)

$$\rho_{mn,y} = e^{-b_{mn}}.$$
(3)

For the model implemented in this research, the cross-correlation has been assumed to be constant across all spectral wavelengths and for all classes.

C. Solar and Atmospheric Effects

The solar and atmospheric effects model converts the scene reflectance to the spectral radiance received by the sensor. The computer code Lowtran 7 [12] is used to compute the radiances and transmittances. Equation (4) shows the form of the model for the spectral radiance vector L_λ received by the sensor.

$$L_\lambda = L_{\lambda,S} * X + L^0_{\lambda,\text{Path}} + \left[L^1_{\lambda,\text{Path}} - L^0_{\lambda,\text{Path}}\right] * X_A.$$
(4)

The symbol * is used here to denote a term by term multiplication of the spectral vectors. X is the surface reflectance vector in the sensor ground instantaneous field of view (IFOV), while X_A is the average reflectance around this area and represents the contribution of the adjacent surface to the received radiance. For this model, the adjacent reflectance X_A is considered to be the average reflectance of all K classes. It is also considered to be uncorrelated with the reflectance within the sensor IFOV since it represents an average over a broad spatial area. $L^1_{\lambda,\text{Path}}$ and $L^0_{\lambda,\text{Path}}$ are the path spectral radiance vectors for surface albedos of 1 and 0,
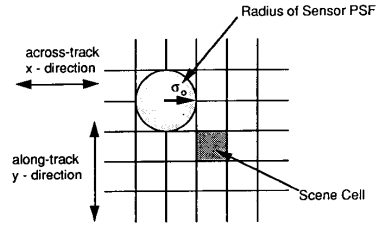

Fig. 4.   Spatial model configuration example for $\sigma_o = 1$ scene cell.

respectively. $L_{\lambda,S}$, the spectral radiance reflected from a perfectly reflecting surface, is as shown in (5).

$$L_{\lambda,S} = \frac{1}{\pi}E_{\lambda,\text{Total}} * T_{\lambda,\text{Atm}}.$$
(5)

Here $E_{\lambda,\text{Total}}$ is the total solar spectral irradiance vector incident at the surface and $T_{\lambda,\text{Atm}}$ is the spectral transmittance vector for the path from the surface to the sensor (calculated by Lowtran). The total irradiance is made up of a direct component (calculated by Lowtran) and a diffuse component. An empirical relationship was developed and used in [10] to compute the total irradiance from the direct component and is shown in (6):

$$E_{\lambda,\text{Total}} = \frac{\cos(\theta_{\text{solar}})E_{\lambda,\text{Direct}}}{\exp[-K_D\tau_\lambda]}.$$
(6)

K_D is the diffuse irradiance constant with values ranging from 0.75 to 1.25 for increasing adjacent surface reflectance, and τ_λ is the total optical path length. θ_{solar} is the solar zenith angle as measured from directly above the scene.

After the application of the atmospheric effects function, the mean and covariance of the signal radiance are as follows. The mean spectral radiance is given by (7):

$$\overline{L_\lambda} = L_{\lambda,S} * \overline{X} + L^0_{\lambda,\text{Path}} + L^{1-0}_{\lambda,\text{Path}} * \overline{X_A}.$$
(7)

$L^{1-0}_{\lambda,\text{Path}}$ is the difference between the path radiances for a surface albedo of 1 and 0. The spectral radiance covariance matrix Σ_{L_λ} is derived as follows for each row m, column n entry $\sigma_{L,mn}$:

$$\sigma_{L,mn} = E\{(L_m - \overline{L_m})(L_n - \overline{L_n})\}$$
(8)

$$= E\left\{ \begin{array}{c} (L_{m,S}X_m + L^0_{m,\text{Path}} + L^{1-0}_{m,\text{Path}}X_{A,m} - L_{m,S}\overline{X_m} - L^0_{m,\text{Path}} - L^{1-0}_{m,\text{Path}}\overline{X_{A,m}}) \\ \cdot(L_{n,S}X_n + L^0_{n,\text{Path}} + L^{1-0}_{n,\text{Path}}X_{A,n} - L_{n,S}\overline{X_n} - L^0_{n,\text{Path}} - L^{1-0}_{n,\text{Path}}\overline{X_{A,n}}) \end{array} \right\}$$
(9)

$$= L_{m,S}\sigma_{X,mn}L_{n,S} + L^{1-0}_{m,\text{Path}}\sigma_{A,mn}L^{1-0}_{n,\text{Path}}$$
(10)

The subscript m denotes the mth entry of the reflectance and radiance vectors. Also, $\sigma_{X,mn}$ is the mnth entry of the reflectance covariance matrix Σ_k, while $\sigma_{A,mn}$ is the mnth entry of the covariance matrix Σ_A of the averaged reflectance, which is given in (11).

$$\Sigma_A = \frac{1}{K^2}(\Sigma_1 + \Sigma_2 + \cdots + \Sigma_K).$$
(11)

In the derivation of Σ_A, the reflectances of the classes averaged together are considered to be uncorrelated with

each other since they are spatially separated as fields in the scene.

D. Sensor Spatial Effects

The spatial effects function uses the results of Mobasseri [11] to modify the spectral radiance covariance matrix. The separable exponential spatial correlation model of (1) is assumed for the scene, along with a Gaussian point spread function (PSF) for the sensor as shown in (12). Fig. 4 shows the relationship between the sensor PSF radius σ_o and the scene cell size.

$$h(x, y) = \frac{1}{2\pi\sigma_o^2} \exp\left(-\frac{x^2 + y^2}{2\sigma_o^2}\right). \qquad (12)$$

Since σ_o is one-half the number of scene cells (on a side) in the sensor ground IFOV, its value must be modified to reflect the change in the ground IFOV as the sensor zenith view angle (θ_{view}) changes. The spatial direction in which this occurs is dependent upon the relative azimuthal angle of the sensor and the ground reference axis. For simplicity, the sensor azimuth is defined to be 0°. Thus in terms of $\sigma_{o,x}$ and $\sigma_{o,y}, \sigma_o$ is projected as in (13) and (14):

$$\sigma_{o,x} = \sigma_o \qquad (13)$$

$$\sigma_{o,y} = \frac{\sigma_o}{\cos(\theta_{\text{view}})}. \qquad (14)$$

Mobasseri [11] defined a weighting matrix W_s that is a function of the spatial model and PSF parameters. Following his results, the sensor spatial response modifies each mn entry in Σ_{L_λ} as in (15):

$$\sigma_{L,mn}^S = W_s^{mn}\sigma_{L,mn} \qquad (15)$$

where

$$W_s^{mn} = 4\exp\left[\left(a_{mn}^2 + b_{mn}^2\right)\sigma_{o,x}\sigma_{o,y}\right]$$
$$\cdot \operatorname{erfc}\left(a_{mn}\sqrt{2}\,\sigma_{o,x}\right)\operatorname{erfc}\left(b_{mn}\sqrt{2}\,\sigma_{o,y}\right) \qquad (16)$$

and erfc($\cdot$) is the complimentary error function defined as in (17).

$$\operatorname{erfc}(\alpha) = \frac{1}{\sqrt{2\pi}}\int_\alpha^\infty e^{-t^2/2}\,dt. \qquad (17)$$

Since the spatial autocorrelation coefficients have been assumed to be constant across spectral wavelengths, the parameter W_s^{mn} is constant for all mn.

Thus (15) gives a new $\Sigma_{L_\lambda}^S$ that represents the spectral radiance covariance matrix after application of the sensor spatial effects. The mean spectral radiance vector is unchanged by the spatial model as shown in (18):

$$\overline{L_\lambda^S} = \overline{L_\lambda}. \qquad (18)$$

E. Sensor Spectral Effects

The sensor spectral effects are applied by a linear transformation matrix B that converts the spectral radiance to the signal levels in each of the sensor image bands. The sensors may be of two types in our model: line scanner sensors such as Landsat TM [1] with spectral bands wider than the wavelength spacing used in the model scene, or imaging spectrometers such as HIRIS [9], which have the same spectral resolution as the model scene. For the line

scanner sensors with L bands, this matrix is L rows by M columns, with each row consisting of the normalized response of that band to each of the M wavelengths of the spectral radiance. Also, each entry in the matrix is multiplied by $\Delta\lambda$, the spectral resolution of the spectral radiance vectors. The resulting signals will be in terms of radiances. Thus this matrix B for line scanner sensors is formed as in (19).

$$B = \Delta\lambda\begin{bmatrix} \text{Band 1 Response} \\ \text{Band 2 Response} \\ \vdots \\ \text{Band } L \text{ Response} \end{bmatrix}_{L \times M.} \qquad (19)$$

For imaging spectrometers with the same spectral resolution as the scene (i.e., $L = M$), the matrix will be diagonal $L \times L$ with the resulting signal in terms of electrons. For either sensor type, the mean received signal vector is thus obtained by

$$\overline{S} = B\overline{L_\lambda^S} \qquad (20)$$

while the signal covariance is as shown in (21):

$$\Sigma_S = B\Sigma_{L_\lambda}^S B^T \qquad (21)$$

F. Sensor Noise Model

The sensor noise effects are modeled as zero mean random processes, except for the deterministic absolute radiometric error e_R and the detector dark current D. These deterministic effects are added directly to the mean signal vector to yield the noisy mean vector $\overline{Y}$ as in (22):

$$\overline{Y} = (1 + e_R)\overline{S} + D. \qquad (22)$$

The random noise sources modeled include shot noise, thermal noise, read noise, quantization error, and relative calibration error. The form of these models was discussed in our earlier paper [10]. Reference [16] discussed how these sources of noise affect the covariance matrix of the signals received by the sensor. The result used here is that while some of the noise sources may be a function of the signal (shot and relative calibration error), they are still uncorrelated with the signal and the variances add directly. Also, each noise source is assumed to be independent of the others and uncorrelated from spectral band to spectral band. Thus the signal covariance is modified as in (23):

$$\Sigma_Y = (1 + e_R)^2\Sigma_S + \Lambda_{\text{therm}} + \Lambda_{\text{shot}} + \Lambda_{\text{read}} + \Lambda_{\text{quant}} + \Lambda_{\text{cal}}. \qquad (23)$$

Here, the Λ's are diagonal matrices with each entry being the variance of that noise source for that sensor band.

G. Feature Extraction

Feature extraction is optionally applied by combining the sensor bands according to a weighting matrix F to create the features with mean $\overline{Z}$ and covariance Σ_Z as in (24) and (25):

$$\overline{Z} = F\overline{Y} \qquad (24)$$

$$\Sigma_Z = F\Sigma_Y F^T. \qquad (25)$$

To transform the L-dimensional vectors Y to the N-dimensional feature space, F is N rows by L columns of weighting coefficients. For a spectral feature compression

scheme based on combining spectral bands, these coefficients are just 0 and 1 to appropriately skip or select the sensor bands.

H. Pairwise Error and Multiclass Classification Accuracy Estimation

After the class statistics of each class have been modified by the above functions, an estimate of the probability of error is made. Reference [13] discussed a pairwise error estimate based upon the class mean and covariance statistics and found it to be closely related to the actual classification error. Equation (26) shows this estimate of probability of error P_e, which uses the Bhattacharyya distance B_{kl} between classes k and l defined below.

$$P_e^{kl} = \text{erfc}\left\{\sqrt{2B_{kl}}\right\}. \tag{26}$$

The function $\text{erfc}(\cdot)$ was defined earlier. The Bhattacharyya distance B_{kl} between class k and class l with mean vectors $\overline{Z}_k$ and $\overline{Z}_l$, and covariance matrices Σ_k and Σ_l, is given in (27):

$$B_{kl} = \frac{1}{8}\left(\overline{Z}_k - \overline{Z}_l\right)^T\left(\frac{\Sigma_k + \Sigma_l}{2}\right)^{-1}\left(\overline{Z}_k - \overline{Z}_l\right)$$

$$+ \frac{1}{2}\log_e\left[\frac{\left|\frac{\Sigma_k + \Sigma_l}{2}\right|}{\sqrt{|\Sigma_k||\Sigma_l|}}\right]. \tag{27}$$

Reference [13] also discussed an upper bound on the probability of error in the multiclass case as being the sum of the pairwise error estimates. Thus in our model the following estimate for the multiclass classification accuracy $\hat{P}_c$ (in percent) is used.

$$\hat{P}_c = 100\left[1 - \sum_{k=1}^{K}\sum_{l=1 \neq k}^{K} P_e^{kl}\right]. \tag{28}$$

Since the summation of the pairwise errors is an upper bound, this estimate of the classification accuracy will be pessimistic in multiclass experiments.

An error estimation technique for the multiclass multivariate Gaussian classification problem was presented by Mobasseri and McGillem [21]. This estimate was based upon class statistics also, but utilized a combined analytical and numerical integration technique to provide a nearly exact estimate of the Bayes error. This algorithm was not utilized in our present work due to computational considerations and the desire to maintain the analytic nature of the model, although it could be implemented as an extension.

I. Comparison Between Analytical and Simulation Models

The analytical model described here offers the advantages of being simpler and computationally more efficient than the simulation model described in [10]. However, its representation of the real world is less accurate. Table I lists several factors that the analytical model is not able to represent at present.

These factors can be significant. The following section presents some results of comparing the accuracy estimate of the analytical and simulation models.

TABLE I
SYSTEM FACTORS NOT INCLUDED IN ANALYTICAL MODEL

Size and Spatial Arrangements of Fields
Mixed Pixels at Field Borders
Non-Gaussian Sensor PSF
Training Field Selection and Size

TABLE II
KANSAS WINTER WHEAT DATA SET

Location: Date:	Finney County, Kansas May 3, 1977	
Spectral Classes	Number of Fields	Number of Samples
Winter Wheat	25	658
Summer Fallow	6	211
Unknown	39	682

Another difference between the modeling approaches is that the analytical model works in a parametric space, while the simulation model produces multispectral images that can be displayed and processed like real ones. This attribute of the simulation approach is useful for the development of processing algorithms when "real" data is not available or when images of controllable characteristics are desired.

IV. INSIGHTS INTO THE REMOTE SENSING PROCESS

In this section we discuss the application of the system model to the radiometric and classification performance of a typical remote sensing system. We begin by describing the scene and other system parameters and then compare the performance of the simulation and analytical models for the same system description. The results of investigating trends using the analytical model are next presented as well as results of investigating the interrelated effects of several parameters.

A. Baseline System Description

In this investigation of a typical remote sensing system we utilized a baseline scene, sensor, and processing description. The spectral statistics of the scene were based upon the field data described in Table II. This data set was obtained from the LARS field database [17].

Table III shows the significant system parameters used as the baseline in these experiments. The sensor used was a model version of the HIRIS instrument. Reference [18] contains a full description of this model. The feature selection was performed using the Spectral Feature Design (SFD) algorithm described in reference [19].

B. Performance Comparison Between the Analytical and Simulation Models

To evaluate the performance of the analytical model, a comparison was made to a similarly defined system using the simulation model. In the simulation model a square scene was defined and split down the middle with the Summer Fallow and the Unknown classes of Table II assigned to opposite sides. 100% of the samples from each class were used in the training and the test of the simulation Maximum Likelihood classifier. For each of these experiments, the simulation model was run five times and the resulting accu-

TABLE III
BASELINE CONFIGURATION FOR SYSTEM PARAMETER STUDIES

Scene	
Surface Meteorological Range	16 km
Atmospheric Model	1976 US Standard
Haze Parameter	Rural Extinction
Diffuse Irradiance Constant	0.84
Solar Zenith Angle	30°
View Zenith Angle	0°
Ground Size of Scene Cell	15 m
Across-Track Spatial Correlation Coefficient	0.6
Along-Track Spatial Correlation Coefficient	0.6
Sensor (HIRIS MODEL)	
Spatial Radius	
Analytical Model σ_o	1 Scene Cell
Simulation Model Ground IFOV	30 m
Read Noise Level	Nominal
Shot Noise Level	Nominal
IMC Gain State	1
Relative Calibration Error	0.5%
Absolute Radiometric Error	0%
Radiometric Resolution	12 Bits
Processing	
Feature Extraction	Six Features Derived From Spectral Feature Design Algorithm

TABLE IV
CLASSIFICATION ACCURACY OF BASE SYSTEM CONFIGURATION

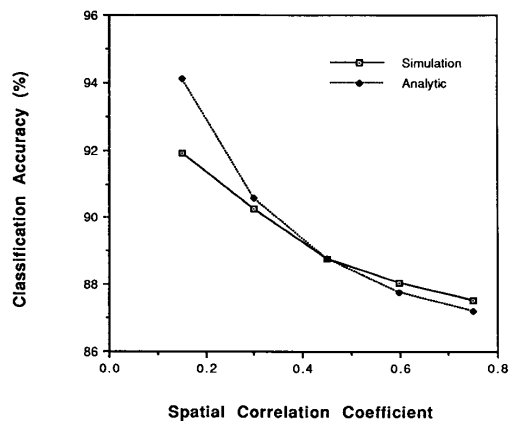| Simulation Model	88.06%
Analytical Model	87.78%

Fig. 5. Classification accuracy versus scene spatial correlation coefficient.

TABLE V
INCREMENTS USED IN GROUND SIZE EXPERIMENT

Ground Size of Scene Cell	Resulting Size of Simulated Image	Radius of Analytic Sensor PSF (σ_o)
30 Meters	80 rows by 80 columns	0.5 cells
15 Meters	40 rows by 40 columns	1.0 cell
7 Meters	20 rows by 20 columns	2.0 cells
4 Meters	10 rows by 10 columns	4.0 cells
2 Meters	5 rows by 5 columns	8.0 cells

racies averaged together to reduce the effects of the random number generators. The classification accuracy shown for the simulation model is the average of the two individual class accuracies.

For the base system configuration shown in Table III, the accuracies obtained are shown in Table IV. The values are within 1% of each other, indicating that, at least for this configuration, the simulation model and the analytic model predict similar performance.

An experiment was performed to compare the effect on classification accuracy of the spatial model parameters. Fig. 5 shows the result of changing the spatial correlation coefficient $\rho = \rho_x = \rho_y$ of the scene cells. In the simulation model the data were synthesized to have the desired correlation coefficient by the use of the autoregressive model described in [10]. For this experiment the ground size of the scene cells was held constant.

As can be seen, the simulation model and the analytical model track the change in accuracy due to the spatial correlation. These curves support the work in [11] on analyzing the effect of the spatial model on class spectral statistics through the weighting function described in (16).

Another comparison experiment of the spatial model was performed by allowing the ground size of the scene cells to change and observing the effect on classification performance. The change in scene cell size for the simulation model is equivalent to changing the PSF radius of the analytical model. Table V presents the increments used in this experiment. The ground IFOV of the sensor was held constant at 30 m in the simulation model. The spatial correlation coefficient also was held constant.

Fig. 6 shows the results of this experiment. At large scene cell sizes both models show an increase in accuracy as the scene cell size decreases. However, while the analytical model continues this trend at cell sizes less than 10 m, the simulation model shows a reduction in accuracy due to the effects of mixed pixels at the border between the classes and reduced training set size.
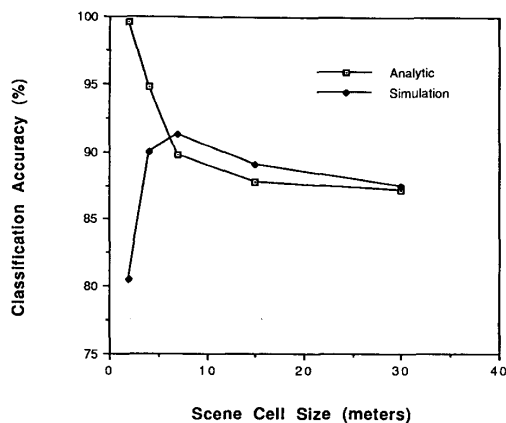
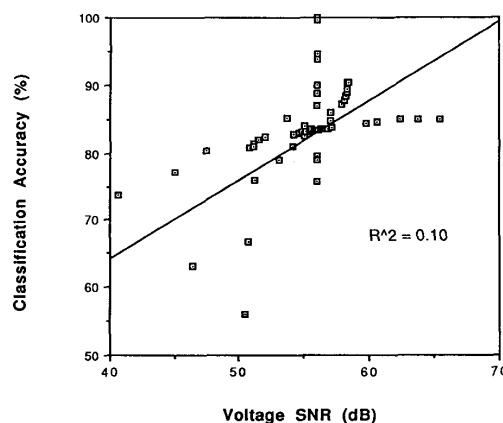Fig. 6. Classification accuracy versus ground size of scene cells.

Fig. 7. Accuracy versus voltage SNR for system parameter experiments.

TABLE VI
SUMMARY OF RESULTS FOR SYSTEM PARAMETER EXPERIMENTS

System Parameter (Increasing) Scene	Voltage SNR	Power SNR	Accuracy
Spatial Correlation	No Change	Increase	Decrease
Meteorological Range	Increase	Increase	Increase
Solar Zenith Angle	Decrease	Decrease	Decrease
View Zenith Angle	Decrease	Decrease	Increase
Sensor			
PSF Radius	No Change	Decrease	Increase
Shot Noise	Decrease	Decrease	Decrease
Read Noise	Decrease	Decrease	Decrease
IMC Gain	Increase	Increase	Increase
Radiometric Resolution	Increase	Increase	Increase
Relative Calibration Error	Decrease	Decrease	Decrease
Absolute Radiometric Error	Increase	Increase	Increase
Processing			
Number of Features	Increase	Increase	Increase

C. System Parameter Effects on Radiometric and Classification Performance

A sequence of experiments varying one of the system parameters and observing the effect on radiometric performance and classification accuracy was performed and reported in [14]. A summary of these results is shown in Table VI. The scene classes and baseline system parameters were as shown in Tables II and III. The voltage signal-to-noise ratio (SNR) was calculated at the output of the model sensor and represents the ratio of the signal mean and noise standard deviation levels, while the power SNR is computed as the ratio of the signal variance to noise variance at the output of the sensor. Reference [15] describes these radiometric performance measures in detail.

In Fig. 7 the results of these experiments are displayed quantitatively in a scatter plot to show the relationships between classification accuracy and SNR. A linear regression line is also plotted along with the resulting correlation coefficient $R^2 = 0.10$.

While there appears to be a trend of higher classification accuracy resulting from higher SNR, it is not very significant. The spatial correlation and sensor PSF radius are cases in point. These spatial parameters are used in the sensor model only to modify the signal covariance matrix, and thus they

have no effect on voltage SNR. While their variation had a significant effect on both classification accuracy and power SNR, the effects were opposite. An increase in the correlation of the scene cells within the sensor ground IFOV leads to an increase in the class spectral variances through the weighting function of (16), and thus increased class overlap in the feature space and the resulting decreased classification accuracy. An increase in the sensor PSF radius results in an "averaging" of within class spectral radiance variations, reduced class overlap and thus increased classification accuracy. The classification accuracy is ultimately dependent upon the relationships between the first- and second-order class statistics, not the particular noise level.

D. Interrelationships of System Parameter Effects

In this section we present results of investigating the interrelationships among several system parameters. These results provide insights into the remote sensing process modeled as a system. The analytical model was used for these experiments with the spectral statistics of the three classes of Table II and the system configuration of Table III.

In Fig. 8, we show the effect of surface dependence in the path radiance model for the case of no sensor noise present (to isolate the surface dependence effect). The dotted line was obtained using the atmospheric model as described in this paper, while the solid lie was obtained without the averaged reflectance mean and covariance terms in (7) and (10).

Without the surface dependence of the path radiance the effect of the atmosphere is just a linear transformation of the spectral statistics, resulting in little change in accuracy even in hazy atmospheres. However, with the introduction of the adjacent surface reflectance dependence in the path radiance, the effect of hazy atmospheres on classification accuracy is quite dramatic.

The next experiment investigates the effect of the atmosphere on performance versus view zenith angle. Fig. 9 shows the result. In clear atmospheres the accuracy is seen to increase slightly with viewing angle. This occurs due to the averaging effects of increased ground size of the sensor IFOV as the sensor look angle increases. The reduced varia-
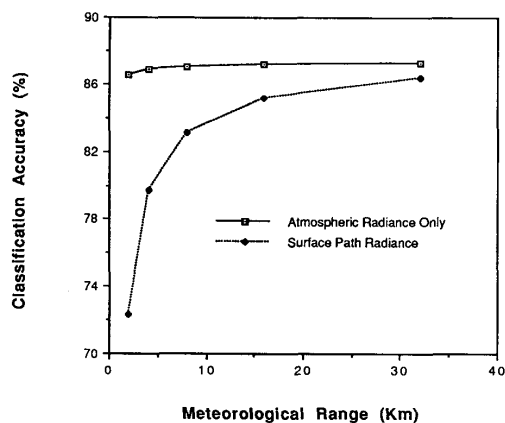
Fig. 8. Effect of surface-dependent path radiance on classification accuracy for several meteorological ranges, with no sensor noise present.
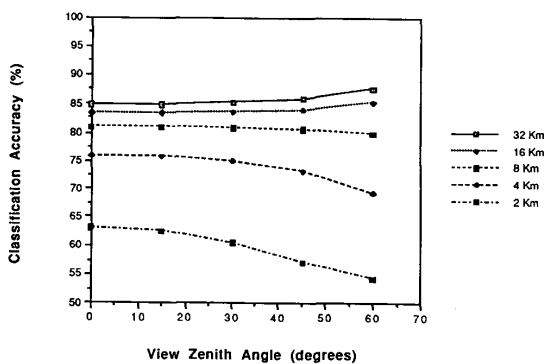

Fig. 9. Effect of meteorological range on view angle for $\theta_{solar} = 30°$.
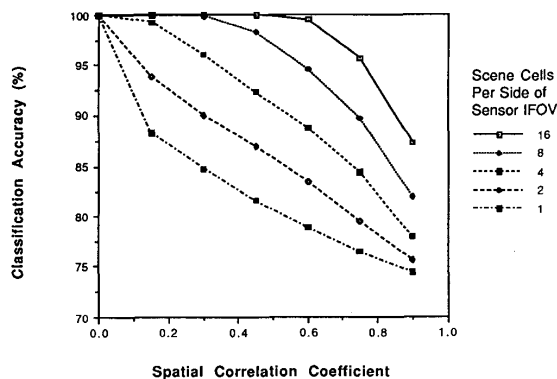

Fig. 10. Effect of scene cell size and spatial correlation coefficient on classification accuracy. The various curves are for differing numbers of ground scene cells contained in one side of the sensor IFOV.

scenes with small areas of constant reflectance the accuracy is more susceptible to correlation changes at high values.

The results of Fig. 10 show what happen for arbitrary combinations of cell size and correlations; however, it is interesting to consider them for more realistic situations. It has been observed that for typical agricultural scenes, spatial correlation generally increases with decreasing scene cell size [14]. That is, for typical data sets, large scene cells have low spatial correlation, while small cells have high correlation. From the summary of results shown in Table VI, the increase in spatial correlation would normally lead to a *decrease* in accuracy, while the decrease in cell size (which is equivalent to an increase in PSF radius) would lead to an *increase* in accuracy. Thus these trends would tend to offset each other. This implies that in typical agricultural scenes the spatial size and correlation of the surface cells have relatively little effect on classification accuracy.

tion in the class spectral statistics leads to greater class separability and higher classification accuracies.

In hazy atmospheres the reduced signal levels and increased additive path radiance (resulting in higher sensor shot noise) lead to lower accuracies at the greater view angles. These curves provide an excellent example of the interdependence of system parameter effects.

Fig. 10 shows a complex relationship between the spatial correlation and size of scene cells. This graph explores the effect on classification accuracy for a fixed sensor IFOV (e.g., 32 m), where the size of the scene cells of constant reflectance is varied (e.g., 2–32 m) and the correlation coefficient is varied from 0 to 0.9. The results are for several relative sizes between the scene cell and the ground IFOV of the sensor. With increasing correlation, the accuracy for large cells (few cells per IFOV side) falls sharply before decreasing at a constant rate, while the accuracy for small scene cells (many cells per IFOV side) remains constant before falling sharply at high correlations.

From the theoretical point of view, the implications of this chart are as follows. For scenes that have large areas of constant reflectance the classification accuracy will be more susceptible to correlation changes at low values, while for

V. CONCLUSION

We have presented an analytical model for the study of interrelated effects of parameters in optical remote sensing systems. This model is aimed at studying these effects on the ability of the system to distinguish between ground cover classes. In this model we use field reflectance measurements, accurate atmospheric models, spatial and spectral statistics, detailed sensor models, and accuracy estimation to bring together a comprehensive yet practical systemwide model.

The analytical model developed in this paper was compared to a more detailed and computationally intensive simulation model and was seen to compare quite similarly, except where spatial constraints such as limited field size and boundaries occur.

System parameter effects on radiometric and classification performance were investigated and trends presented for several parameters. It was seen that higher SNR's did not always lead to high classification performance.

System parameter interrelationships were also investigated. It was observed that additive path radiance from the surface can increase the effect of hazy atmospheres, even when no sensor noise is present. We have shown that in clear atmospheres, the reduced size of the image (over constant

surface area) for off-nadir viewing angles can increase classification accuracy, while in hazy atmospheres high view angles result in decreased accuracy. Results were presented on the interrelationships of the spatial correlation of scene cells, their size and their effect on classification accuracy.

These results have been presented to illustrate trends predicted by the model for the system configurations studied. While it is believed that these trends can be extended to similar system configurations, it should not be assumed that they reflect the absolute values to be obtained in the real system.

ACKNOWLEDGMENT

REFERENCES

[1] S. C. Freden and F. Gordon, Jr., "Landsat satellites," chapter 12, in *Manual of Remote Sensing*, R. N. Colwell, Ed., 2nd ed. Falls Church, VA: American Society of Photogrammetry and Remote Sensing, 1983.
[2] *IEEE Trans. Geosc. Remote Sensing*, V. V. Salomonson, Guest Ed., Special Issue on Landsat-4, vol. GE-22, May 1984.
[3] M. Chevrel, M. Courtois, and G. Weill, "The SPOT satellite remote sensing mission," *Photogrammetric Engineering and Remote Sensing*, vol. 47, no. 8, pp. 1163–1171, 1981.
[4] *Proc. IEEE*, Special Issue on Perceiving Earth's Resources From Space, D. A. Landgrebe, Guest Ed., vol. 73, pp. 947–1127, June 1985.
[5] R. E. Arvidson, D. M. Butler, and R. E. Hartle, "Eos: The earth observing system of the 1990's," *Proc. IEEE*, vol. 73, pp. 1025–1030, June 1985.
[6] J. A. Richards, *Chapt. 1, Remote Sensing Digital Image Analysis: An Introduction*. New York: Springer-Verlag, 1986.
[7] W. M. Porter and H. T. Enmark, "A system overview of the airborne visible/infrared imaging spectrometer (AVIRIS)," in *Imaging Spectroscopy II*, G. Vane, Ed. Bellingham, WA: Society of Photo-Optical Instrumentation Engineering, vol. 834, pp. 22–31, 1987.
[8] V. V. Salomonson, W. L. Barnes, P. W. Maymon, H. E. Montgomery, and H. Ostrow, "MODIS: Advanced facility instrument for studies of the earth as a system," *IEEE Trans. Geosc. Remote Sensing*, vol. GE-27, pp. 145–153, Mar. 1989.
[9] A. F. H. Goetz and M. Herring, "The high resolution imaging spectrometer (HIRIS) for Eos," *IEEE Trans. Geosc. Remote Sensing*, vol. GE-27, pp. 136–144, Mar. 1989.
[10] J. P. Kerekes and D. A. Landgrebe, "Simulation of optical remote sensing systems," *IEEE Trans. Geosc. Remote Sensing*, vol. GE-27, pp. 762–771, Nov. 1989.
[11] B. G. Mobasseri, P. E. Anuta, and C. D. McGillem, "A parametric model for multispectral scanners," *IEEE Trans. Geosc. Remote Sensing*, vol. GE-18, pp. 175–179, Apr. 1980.
[12] F. X. Kneizys *et al.*, "Users guide to LOWTRAN 7," AFGL-TR-88-0177, Air Force Geophysical Lab., Bedford, MA, Aug. 1988.
[13] S. J. Whitsitt, "Error estimation and separability measures in feature selection for multiclass pattern recognition," Ph.D. dissertation, School of Electrical Engineering, Purdue Univ., West Lafayette, IN, Aug. 1977.
[14] J. P. Kerekes and D. A. Landgrebe, "Modeling, simulation, and analysis of optical remote sensing systems," Ph.D. dissertation, TR-EE 89-49, School of Electrical Engineering, Purdue Univ., West Lafayette, IN, Aug. 1989.
[15] ____, "Parameter tradeoffs for imaging spectroscopy systems,"
IEEE Trans. Geosc. Remote Sensing, to be published.
[16] D. A. Landgrebe and E. R. Malaret, "Noise in remote sensing systems: The effect on classification error," *IEEE Trans. Geosc. Remote Sensing*, vol. GE-24, pp. 294–300, Mar. 1986.
[17] L. L. Biehl, M. E. Bauer, B. F. Robinson, C. S. T. Daughtry, L. F. Silva, and D. E. Pitts, "A crops and soils data base for scene radiation research," in *Proc. 8th Int. Symp. on Machine Processing of Remotely Sensed Data*, pp. 169–177, Purdue Univ., West Lafayette, IN, 1982.
[18] J. P. Kerekes and D. A. Landgrebe, "HIRIS performance study," TR-EE 89-23, School of Electrical Engineering, Purdue Univ., West Lafayette, IN, Apr. 1989.
[19] C.-C. Chen and D. A. Landgrebe, "A spectral feature design system for the HIRIS/MODIS era," *IEEE Trans. Geosc. Remote Sensing*, vol. GE-27, pp. 681–686, Nov. 1989.
[20] K. S. Fu, D. A. Landgrebe, and S. Phillips, "Information processing of remotely sensed agricultural data," *Proc. IEEE*, vol. 57, pp. 639–653, Apr. 1969.
[21] B. G. Mobasseri and C. D. McGillem, "Multiclass Bayes error estimation by a feature space sampling technique," *IEEE Trans. Syst. Man Cybern.*, vol. SMC-9, pp. 660–665, Oct. 1979.

John P. Kerekes (S'83–M'83) was born in South Bend, IN. He received the B.S.E.E., M.S.E.E., and Ph.D. degrees from Purdue University, West Lafayette, IN, in 1983, 1986, and 1989, respectively.

From 1983 to 1984 he was a member of the technical staff of the Space and Communications Group of the Hughes Aircraft Co., El Segundo, CA, where he performed circuit design for communications satellites. From 1984 to 1989 he was a Graduate Teaching Assistant in the School of Electrical Engineering at Purdue University. From 1986 to 1989 he was a Graduate Research Assistant, working with both the School of Electrical Engineering and the Laboratory for Applications of Remote Sensing. He is presently employed by the Massachusetts Institute of Technology Lincoln Laboratory, Lexington, MA.

Dr. Kerekes is a member of Phi Kappa Phi, Tau Beta Pi, and Eta Kappa Nu.

David A. Landgrebe (S'54–M'57–SM'74–F'77) received the B.S.E.E., M.S.E.E., and Ph.D. degrees from Purdue University, West Lafayette, IN.

He is Professor of Electrical Engineering at Purdue University. His area of speciality in research is communication science and signal processing, especially as applied to Earth observational remote sensing. His research contributions to that field have been in the areas of multispectral pattern recognition, spectral/spatial/temporal classifiers, spectral feature design, and system simulation. He is also co-author of the text, *Remote Sensing: The Quantitative Approach*, and a contributor to the book, *Remote Sensing of Environment*, and the *ASP Manual of Remote Sensing* (1st ed.). He has been a member of the editorial board of the journal *Remote Sensing of Environment* since its inception, and is also on the editorial board of the journal *Image and Computer Vision*.

Dr. Landgrebe is a member of the American Society of Photogrammetry and Remote Sensing, the American Association for the Advancement of Science, and the American Society of Engineering Education. He is also a member of the Eta Kappa Nu, Tau Beta Pi, and Sigma Xi honor societies. He has received both of the outstanding teacher awards given by his department. He has also received the NASA Exceptional Scientific Achievement Medal for his work in the field of machine analysis methods for remotely sensed Earth observational data. He was President of the IEEE Geoscience and Remote Sensing Society during 1986 and 1987 and has been a member of its' Administrative Committee since 1979.